Effect of Data Acquisition and Analysis Method on Fiber Orientation Estimation in Diffusion MRI

Bryce Wilkins, Namgyun Lee, Vidya Rajagopalan, Meng Law, and Natasha Leporé

Abstract In this paper we investigate the effect of single-shell q-space diffusion sampling strategies and applicable multiple-fiber analysis methods on fiber orientation estimation in Diffusion MRI. Specifically, we develop a simulation based on an in-vivo data set and compare a two-compartment "ball-and-stick" model, a constrained spherical deconvolution approach, a generalized Fourier transform approach, and three related methods based on transforms of Fourier data on the sphere. We evaluate each method for $N = 20$, 30, 40, 60, 90 and 120 angular diffusion-weighted samples, at $\text{SNR} = 18$ and diffusion-weighting $b = 1{,}000\,\text{s/mm}^2$, common to clinical studies. Our results quantitatively show the methods are most distinguished from each other by their fiber detection ability. Overall, the "ball-and-stick" model and spherical deconvolution approach were found to perform best, yielding the least orientation error, and greatest detection rate of fibers.

B. Wilkins (✉)
Department of Biomedical Engineering, University of Southern California, Los Angeles, CA, USA
e-mail: brycewil@usc.edu

N. Lee
Center of Magnetic Resonance Research, Korea Basic Science Institute, Ochang, South Korea

Department of Biomedical Engineering, University of Southern California, Los Angeles, CA, USA
e-mail: namgyunl@kbsi.re.kr

V. Rajagopalan · N. Leporé
Department of Radiology, Children's Hospital of Los Angeles, Los Angeles, CA, USA
e-mail: vrajagopalan@chla.usc.edu; nlepore@chla.usc.edu

M. Law
Department of Radiology, Keck School of Medicine of USC, Los Angeles, CA, USA
e-mail: meng.law@med.usc.edu

T. Schultz et al. (eds.), *Computational Diffusion MRI and Brain Connectivity*,
Mathematics and Visualization, DOI 10.1007/978-3-319-02475-2_2,

1 Introduction

Diffusion-weighted Magnetic Resonance Imaging (DW-MRI) uniquely reveals the complex white-matter pathways of the human-brain, in-vivo. As such, DW-MRI has been enthusiastically applied to a broad range of clinical and neuroscience research, including analysis of brain trauma [8], assessment of neurological diseases such as Alzheimer's disease [4], and mapping the human brain connectome [10].

In recent years, advances in DW-MRI have led to a variety of diffusion sampling strategies and many alternative analysis methodologies which aim to reveal the complex nature of white-matter tissue microstructure, such as intra-voxel crossing fiber bundles. For the researcher, it can be very difficult to choose among the acquisition and analysis methods available without detailed knowledge of their strengths and weaknesses, and as a result data may be sub-optimally processed.

In this paper we quantitatively compare the following six multiple-fiber diffusion analysis methods: a two-compartment "ball-and-stick" model (BSM) [3], a (non-negativity) Constrained Spherical Deconvolution (CSD) approach [11], a generalized Fourier transform method known as Generalized q-sampling Imaging (GQI) [14], and three related approaches based on transforms of Fourier data on the sphere (analytical Q-Ball Imaging (QBI) [6], Funk-Radon and Cosine Transform (FRACT) QBI [7], and Constant Solid Angle (CSA) QBI [1]).

We evaluate these methods by developing a ground-truth of fiber orientations from in-vivo brain data, and then synthesize the diffusion-weighted signal. After processing the synthetic data by each of the methods, we compare results in terms of fiber detection accuracy and individual fiber orientation error. We focus our study on a SNR and diffusion-weighting common to Diffusion Tensor Imaging (DTI) [2], as DTI remains the primary diffusion acquisition scheme used in routine clinical neuro-radiological imaging sessions.

2 Materials and Methods

2.1 *Diffusion-Weighted Data Synthesis*

A diffusion-weighted dataset was synthesized according to a multi-tensor model accommodating three fibers per voxel in addition to a free-diffusion compartment. For any given voxel, the signal model is:

$$S\left(b, \mathbf{g}_j\right) = S_0\left[f_0 \exp\left(-bD_0\right) + (1-f_0)\sum_{k=1}^{3} f_k \exp\left(-b\mathbf{g}_j^{\top}\mathbf{D}_k\mathbf{g}_j\right)\right] \qquad (1)$$

where S_0 simulates T_2-weighting, f_0 and D_0 are the volume fraction and diffusivity, respectively, of the isotropic free-diffusion compartment, f_k and $\mathbf{D}_k$ are the volume fraction and diffusion tensor, respectively, of the kth fiber in the voxel, b is the diffusion-weighting, and $\mathbf{g}_j$ is a unit vector representing the jth diffusion sampling direction. Altogether the volume fractions satisfy $f_0 + (1 - f_0) \sum_{k=1}^{3} f_k = 1$.

Each fiber's tensor was computed from a rotated single tensor model according to $\mathbf{D}_k = \mathbf{R}_\mathbf{x}(\mathbf{v})\,\mathbf{D}_\mathbf{x}\mathbf{R}_\mathbf{x}(\mathbf{v})^\top$, where $\mathbf{v}$ is a vector defining the desired fiber orientation, and $\mathbf{R}_\mathbf{x}(\mathbf{v})$ is the rotation matrix to rotate the vector $[1\ 0\ 0]^\top$ oriented along the x-axis, to along $\mathbf{v}$. The single fiber tensor is:

$$\mathbf{D}_\mathbf{x} = \begin{bmatrix} \lambda_1 & 0 & 0 \\ 0 & \lambda_2 & 0 \\ 0 & 0 & \lambda_3 \end{bmatrix} \tag{2}$$

Complex Gaussian noise was added to the synthesized DW signal (1) to achieve a Rician distribution of noisy magnitude diffusion data:

$$E\left(b, \mathbf{g}_j\right) = \sqrt{\left(S\left(b, \mathbf{g}_j\right) + \frac{n_1}{\sqrt{2}}\right)^2 + \left(\frac{n_2}{\sqrt{2}}\right)^2} \tag{3}$$

where n_1 and n_2 are independent and identically distributed pseudorandom Gaussian variables with zero mean and standard deviation $\sigma_n = \mu_{S_0}/\mathrm{SNR}$, in which μ_{S_0} is the mean signal from a homogeneous white-matter region of the S_0 image, and SNR is the desired signal-to-noise ratio of the magnitude data.

2.2 Quantitative Metrics

After processing the synthesized data, the accuracy of fiber estimation was quantitatively determined in terms of individual fiber orientation error, and accuracy of fiber detection.

2.2.1 Fiber Orientation Error

The fiber orientation error is the angular separation between pairs of estimated and actual fiber directions, and lies in the range 0–90°. In this study, we report individual orientation errors for the pairing of estimated and actual fibers that yields the minimum total error on a voxel-by-voxel basis. Each estimated fiber is paired with only one actual fiber.

2.2.2 False-Positive and False-Negative Rate

The number of incorrect fibers (either false-positives corresponding to spurious fiber orientations, or false-negatives corresponding to missing true fiber orientations) was recorded as the difference between the number of estimated and actual fibers on a voxel-by-voxel basis. Upon summing over all similar voxels (those with 1, 2 or 3 fibers in the ground-truth) the false-positive (negative) rate is the number of spurious (missing) fibers, as a percentage of the actual number of fibers present.

3 Application: Comparison of Fiber Estimation of Several Diffusion Analysis Methods

We use the simulation framework of Sect. 2 to compare the performance of several diffusion analysis methods. In the following sections we describe how the ground-truth of fiber orientations were determined from in-vivo data, mention parameters of the data synthesis and analysis, and present results.

3.1 Establishment of Ground-Truth

A 28-year-old right-handed male volunteer without any history of neurological disease was scanned on a GE 3T HDxt scanner (General Electric, Milwaukee, WI, USA), equipped with an 8-channel head coil. The subject signed an informed consent form approved by the Institutional Review Board of the University of Southern California.

Diffusion-weighted images were acquired by a twice-refocused pulsed-gradient spin-echo sequence with TE/TR = 83.4/16,100 ms, matrix = 128×128, ASSET acceleration factor of 2, voxel size = 2.4 × 2.4 × 2.4 mm, 60 contiguous slices, 150 diffusion gradient directions with diffusion-weighting $b = 1{,}000\,\mathrm{s/mm^2}$, and 10 non-diffusion weighted images. The acquisition took approximately 43 min.

The diffusion data was processed by the FSL [9] probabilistic multiple-fiber method BEDPOSTX estimating up to three fibers per voxel; default options were used in running BEDPOSTX. A threshold of 0.10 was applied to second and third fiber volume fractions to reduce the possibility of minor fibers as a result of data over-fitting.

The estimated fiber volume fractions (f_1, f_2, f_3) and orientations $(\mathbf{v_1}, \mathbf{v_2}, \mathbf{v_3})$, for each voxel, constituted the utilized output from BEDPOSTX. Because of differences between the BEDPOSTX multi-fiber signal model, and that used for data synthesis (1) the isotropic compartment fraction determined by BEDPOSTX was not used. Instead, the fiber fractions were normalized $(\sum_{k=1}^{3} f_k = 1)$ and f_0 was iteratively determined on a voxel-by-voxel basis by systematically adjusting its value until the generalized fractional anisotropy (GFA [13]) of the synthetic data matched that of the in-vivo data to within a tolerance of 0.00005.

Also, an anatomical $\mathrm{T_1}$-weighted SPGR image (TE/TR = 2.856 ms/7 ms) was acquired with resolution 1 × 1 × 1 mm. This image was registered to the mean

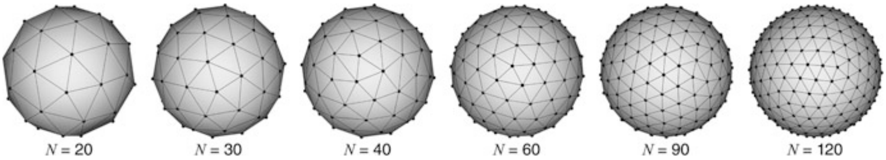

Fig. 1 Diffusion sampling patterns used for data synthesis and analysis. In each case, the number of vertices on the sphere is *twice* the number of diffusion-weighting directions, N, due to the symmetry of diffusion (a measurement in direction $\mathbf{g} = [g_x\ g_y\ g_z]^\top$ is equivalent to a measurement in direction $-\mathbf{g}$)

non-diffusion weighted image and subsequently segmented into white-matter (WM), gray-matter (GM) and cerebrospinal fluid (CSF) using default options in SPM. The tissue probability maps were down-sampled by linear interpolation to the resolution of the DW images, and each voxel was classified as WM, GM, or CSF according to its most probable tissue type.

3.2 Data Synthesis

Parameters for the single-fiber tensor and diffusivity of the free diffusion compartment were obtained from DTI analysis of the in-vivo data (Sect. 3.1). Approximately 250 voxels classified as WM and having $0.85 \leq \mathrm{FA} \leq 0.95$ were used to determine eigenvalues $\{\lambda_1, \lambda_2, \lambda_3\} = \{1.70, 0.17, 0.17\} \times 0.001\mathrm{mm}^2/\mathrm{s}$ ($\mathrm{FA} = 0.89$) for the single-fiber tensor model. The free diffusion parameter D_0 was computed for each tissue compartment by averaging mean diffusivity over similarly classified voxels, resulting in $\{D_0^{\mathrm{WM}}, D_0^{\mathrm{GM}}, D_0^{\mathrm{CSF}}\} = \{0.68, 0.96, 2.25\} \times 0.001\mathrm{mm}^2/\mathrm{s}$.

To evaluate the effect of angular sampling on fiber estimation, we evaluated six sampling patterns consisting of $N = 20$, 30, 40, 60, 90 and 120 pairs of angular samples. The sampling directions were based on minimization of electrostatic energy of antipodal pairs of charged particles on the sphere, as computed by Cook et al. [5] and are shown in Fig. 1.

For each sampling pattern, four data sets were generated with $b = 1{,}000\,\mathrm{s/mm}^2$ and independent noise realization according to (3), to yield $\mathrm{SNR} = 18$ in the magnitude data. One noisy non-DW image was simulated for every ten DW images.

3.3 Data Analysis

The synthetic data sets were processed by the six multi-fiber diffusion analysis methods listed in Table 1, alongside parameters experimentally found to give optimal results in each case. For BSM and CSD methods, FSL [9] and mrTrix

Table 1 Summary of analysis methods. For BSM and CSD, the parameters are specified as command line arguments to FSL and mrTrix programs. In the remaining cases, notation from the methods' paper is used. The * indicates super-resolved CSD

	Diffusion-weighting directions, N					
Analysis method	20	30	40	60	90	120
BSM [3]	−nf = 3	−nf = 3	−nf = 3	−nf = 3	−nf = 3	−nf = 3
CSD [11]	−lmax = 6*	−lmax = 8*	−lmax = 8*	−lmax = 10*	−lmax = 12*	−lmax = 12
	−num = 3	−num = 3	−num = 3	−num = 3	−num = 3	−num = 3
	−thresh = 0.30	−thresh = 0.35	−thresh = 0.30	−thresh = 0.35	−thresh = 0.45	−thresh = 0.40
GQI [14]	$\sigma = 1.66$	$\sigma = 1.85$	$\sigma = 1.90$	$\sigma = 1.95$	$\sigma = 2.05$	$\sigma = 2.10$
QBI [6]	$L = 4$	$L = 6$	$L = 6$	$L = 8$	$L = 10$	$L = 12$
	$\lambda = 0.006$	$\lambda = 0.006$	$\lambda = 0.006$	$\lambda = 0.006$	$\lambda = 0.006$	$\lambda = 0.006$
FRACT [7]	$L = 4$	$L = 6$	$L = 6$	$L = 8$	$L = 10$	$L = 12$
	$\lambda = 0.006$	$\lambda = 0.006$	$\lambda = 0.006$	$\lambda = 0.006$	$\lambda = 0.006$	$\lambda = 0.006$
	$\xi = 0.10\rho$	$\xi = 0.40\rho$	$\xi = 0.40\rho$	$\xi = 0.45\rho$	$\xi = 0.45\rho$	$\xi = 0.45\rho$
CSA [1]	$L = 4$	$L = 4$	$L = 4$	$L = 4$	$L = 4$	$L = 4$
	$\delta = 0.01$	$\delta = 0.01$	$\delta = 0.01$	$\delta = 0.01$	$\delta = 0.01$	$\delta = 0.01$

Table 2 Threshold values used in detecting local maxima, in terms of mean value of the applicable spherical function (SDF or ODF)

	Diffusion-weighting directions, N					
Analysis method	20	30	40	60	90	120
GQI	0.92	0.92	0.92	0.92	0.92	0.92
QBI	0.00	0.00	0.00	0.00	0.00	0.00
FRACT	0.30	0.70	0.70	0.70	0.70	0.70
CSA	2.10	1.90	1.75	1.55	1.45	1.33

[12] were used, respectively, for data processing. We implemented the remaining approaches in MATLAB following the formulations given in the references.

Estimated fiber orientations were output directly by FSL [9] and mrTrix [12] for BSM and CSD methods, respectively. For the remaining approaches, fiber orientations were determined from local maxima of spherical functions (either spin distribution functions (SDF) or orientation distribution functions (ODF)), with the use of thresholds to eliminate minor spurious peaks resulting from noise. In all cases, the spherical functions were reconstructed on a 4th-order regular icosahedron tessellation of the sphere with 2,562 vertices. Table 2 summarizes the threshold values used.

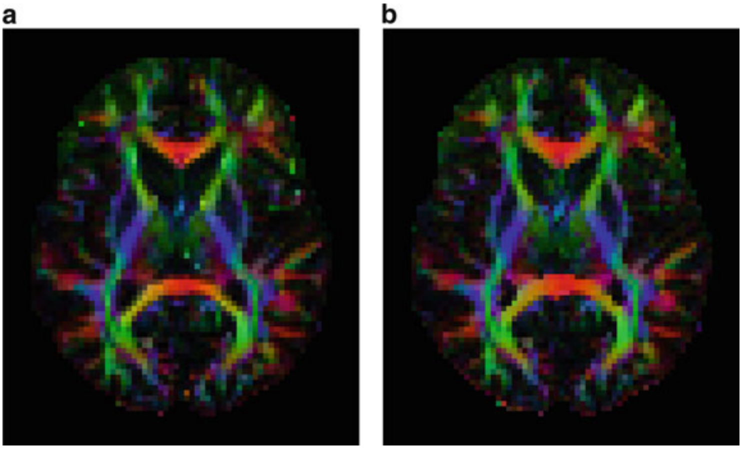

Fig. 2 Comparison of color FA images obtained from DTI analysis of (**a**) the acquired in-vivo data, and (**b**) an example of synthetic noisy data (SNR = 18) generated according to (3) and the fiber parameters established in Sect. 3.1. The data used to obtain (**b**) was simulated using the gradient directions of the in-vivo data

3.4 Results

3.4.1 Comparison of In-Vivo and Synthetic Data

Confidence in the simulation model (1) and fiber directions estimated from the in-vivo data can be established by comparing color FA images, which indicate the primary orientation of white-matter in voxels with a single fiber orientation. Such results obtained from DTI analysis are shown in Fig. 2.

Correspondance between the in-vivo and synthetic data results of Fig. 2 indicates accurate fiber estimation and simulation of the diffusion-weighted signal for the ground-truth directions of the whole brain.

3.4.2 Fiber Orientation Estimation

In the figures that follow, each data point is the mean value over all similar voxels from all independent noise realizations of the quantity indicated. Only voxels satisfying the following criteria in the ground-truth were included in results:

- Voxel must be classified as WM.
- Individual fibers must have a volume fraction of at least 15 %.
- The free-diffusion compartment size is no more than 30 %.

These criteria ensured selection of voxels with reasonable signal from fibers, as compared to free diffusion, from which to estimate fiber orientations.

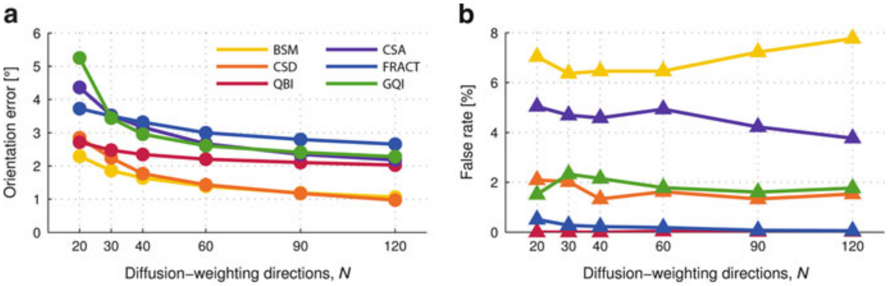

Fig. 3 Single fiber estimation versus number of diffusion-weighting directions, N. Analysis method indicated by color according to the legend. (**a**) Individual fiber orientation error. (**b**) Corresponding false-positive rate

Single Fiber/Voxel Estimation

Figure 3 presents the results of orientation error, and false-positive rate, for voxels containing single fibers in the ground-truth.

As would be expected the BSM method, which most closely matches the data synthesis model (1), had the least fiber orientation error. The CSD approach was also expected to perform well, as the single fiber response function for deconvolution was estimated from a large number of voxels with identical single fiber tensor.

Two Fiber/Voxel Estimation

For voxels with two fibers, results are pooled according to the crossing angle (0–90°) of the two fibers in the ground-truth; 9 bins of width 10° are used. Fiber orientation error and false-negative rate is shown in Fig. 4 grouped by the number of diffusion-weighing directions, N. For clarity, the false-positive rate, which never exceeds a few percent for any data point, is not shown.

Figure 4 shows that as the crossing angle decreases from 90° the orientation error worsens and the false rate heads towards −50 %, at which point only one of the two fibers in each voxel is detected (on average). At small crossing angles (0–20°), the two fibers begin to resemble a single fiber, and as a result the fiber orientation error is small.

Figure 4 also shows that while there may be little separation of methods in terms of orientation error, there can be substantial differences in fiber detection rate. For example, at $N = 60$ and considering the 70–80° crossing angle range, the difference in orientation error between the best and worst methods is approximately 3°, whereas the corresponding difference in false-negative rate is 45 %.

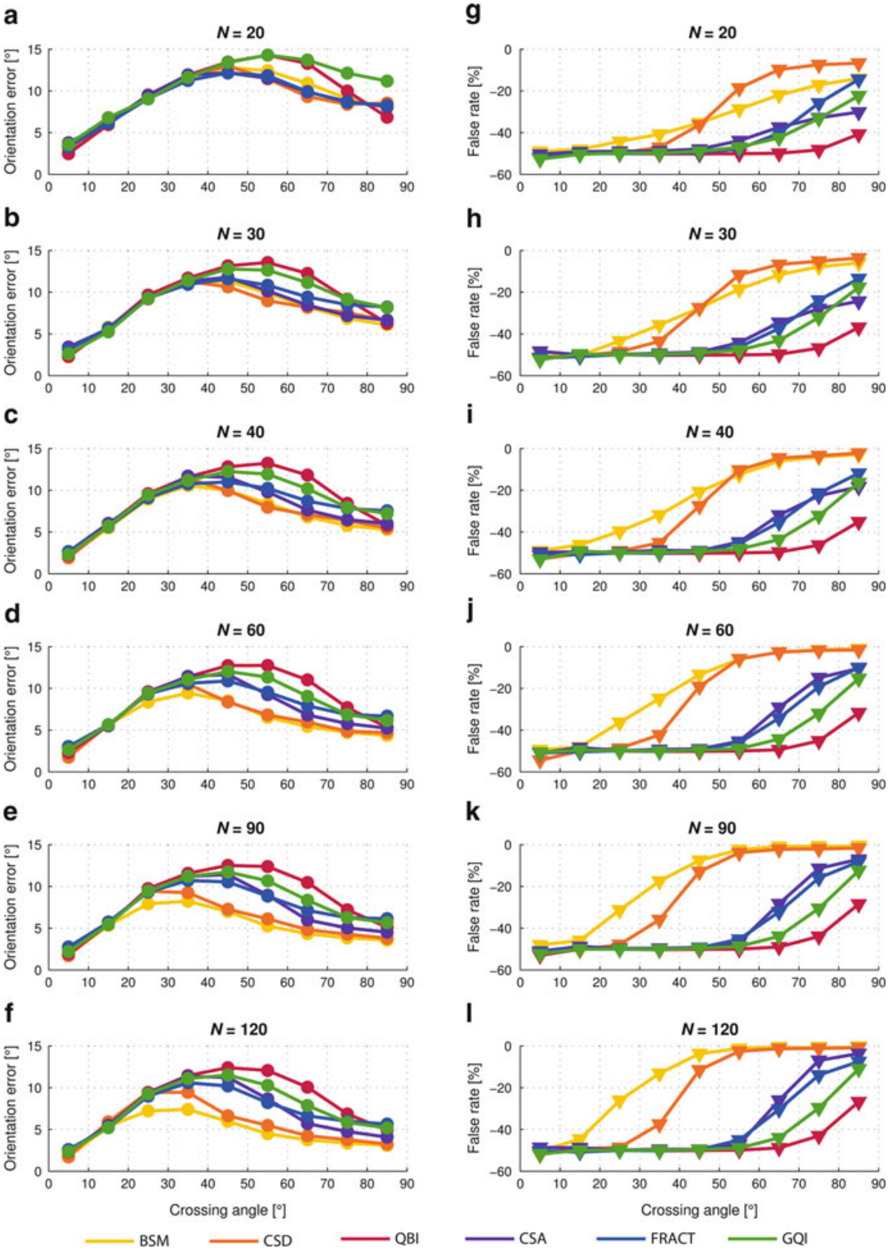

Fig. 4 Two fiber estimation versus fiber crossing angle; analysis method indicated by color according to the legend. (**a**)–(**f**) Individual fiber orientation error, with increasing N. (**g**)–(**l**) Corresponding false-negative rate, with increasing N

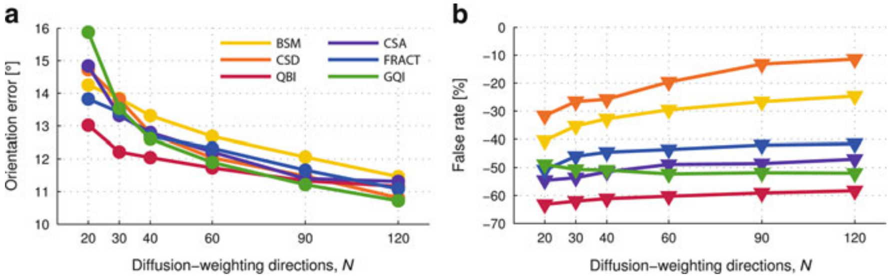

Fig. 5 Three fiber estimation versus number of diffusion-weighting directions, N. Analysis method indicated by color according to the legend. (**a**) Individual fiber orientation error. (**b**) Corresponding false-negative rate

Three Fiber/Voxel Estimation

In the case of three fibers per voxel, wherein each of the fibers are oriented independently of each other and effectively randomly, a single crossing angle is insufficient to describe the relative fiber orientations. However, as the true fiber orientations are known from the ground-truth, we are still able to calculate the orientation error of individual estimated fibers and detect instances of false-negatives. Figure 5 presents the results of individual fiber estimation error, and false-negative rate, for voxels containing three fibers in the ground-truth.

Figure 5 shows that increasing N significantly contributes to reduced orientation error in the case of three fiber orientations per voxel. Unlike the single-fiber results in Fig. 3, in which doubling N from 60 to 120 has little impact on estimation error, there is noticeable improvement here.

We also found substantial differences in detection rate of fibers between the methods, especially with regards to improvement in fiber detection that can be achieved with increasing N; see Fig. 5b.

4 Discussion and Conclusion

In this paper we have examined the accuracy of fiber estimation of six multi-fiber diffusion analysis methods, at a diffusion-weighting of $b = 1{,}000\,\mathrm{s/mm^2}$ and SNR $= 18$, which are common in clinical studies. We also investigated the effect of number of diffusion-weighting directions (from $N = 20$ to 120) on fiber estimation.

Our results reveal the most significant difference between the methods' is their ability to detect multiple fiber orientations. For clinically feasible DW-MRI acquisitions of $N = 20$ to 60 diffusion gradient directions, the two-compartment "ball-and-stick" model (BSM) and constrained (super-resolved) spherical deconvolution (CSD) method yielded the most accurate fiber orientations and greatest detection rate of fibers. While $N = 120$ is typically infeasible for clinical scans because of the time required, the results reveal that such high N is an important factor contributing to the angular resolution necessary for a high detection rate of 3 fibers/voxel.

It is acknowledged that BSM and CSD are favorably biased compared to the remaining methods due to the simulation framework, and so they should not be expected to perform as optimally as is presented here on in-vivo data. However, the relative performance of each method remains unbiased, and the results show more substantial improvements for BSM and CSD as N increases, compared to the remaining methods. For researchers processing DW-MRI data acquired in clinical environments, the results indicate BSM and CSD are the best choices for data analysis in terms of completeness and accuracy of recovering white-matter fiber orientation.

In future work we plan to extend our study with tractography results. This will allow us to investigate the effect of diffusion analysis method on recovering white-matter pathways. Such work will be of interest to researchers undertaking tractography based analysis, including studying brain networks.

References

1. Aganj, I., Lenglet, C., Sapiro, G., Yacoub, E., Ugurbil, K., Harel, N.: Reconstruction of the orientation distribution function in single-and multiple-shell q-ball imaging within constant solid angle. Magn. Reson. Med. **64**, 554–566 (2010)
2. Basser, P.J., Mattiello, J., Le Bihan, D.: Estimation of the effective self-diffusion tensor from the NMR spin echo. J. Magn. Reson. B **103**, 247–254 (1994)
3. Behrens, T.E.J., Woolrich, M.W., Jenkinson, M., Johansen-Berg, H., Nunes, R.G., Clare, S., Matthews, P.M., et al.: Characterization and propagation of uncertainty in diffusion-weighted MR imaging. Magn. Reson. Med. **50**, 1077–1088 (2003)
4. Bozzali, M., Falini, A., Franceschi, M., Cercignani, M., Zuffi, M., Scotti, G., et al.: White matter damage in Alzheimer's disease assessed in vivo using diffusion tensor magnetic resonance imaging. J. Neurol. Neurosur. Ps. **72**, 742–746 (2002)
5. Cook, P.A., Symms, M., Boulby, P.A., Alexander, D.C.: Optimal acquisition orders of diffusion-weighted MRI measurements. J. Magn. Reson. Imaging **25**, 1051–1058 (2007)
6. Descoteaux, M., Angelino, E., Fitzgibbons, S., Deriche, R.: Regularized, fast, and robust analytical q-ball imaging. Magn. Reson. Med. **58**, 497–510 (2007)
7. Haldar, J.P., Leahy, R.M.: Linear transforms for Fourier data on the sphere: application to high angular resolution diffusion MRI of the brain. NeuroImage **71**, 233–247 (2013)
8. Shenton, M.E., Hamoda, H.M., Schneiderman, J.S., Bouix, S., Pasternak, O., Rathi, Y., et al.: A review of magnetic resonance imaging and diffusion tensor imaging findings in mild traumatic brain injury. Brain Imag. Behav. **6**, 137–192 (2012)
9. Smith, S.M., Jenkinson, M., Woolrich, M.W., Beckmann, C.F., Behrens, T.E., Johansen-Berg, H., Bannister, P.R., et al.: Advances in functional and structural MR image analysis and implementation as FSL. NeuroImage **23**, S208–S219 (2004)
10. Sporns, O.: The human connectome: a complex network. Ann. N. Y. Acad. Sci. **1224**, 109–125 (2011)
11. Tournier, J.-D., Calamante, F., Connelly, A.: Robust determination of the fibre orientation distribution in diffusion MRI: non-negativity constrained super-resolved spherical deconvolution. NeuroImage **35**, 1459–1472 (2007)

12. Tournier, J.-D., Calamante, F., Connelly, A.: MRtrix: diffusion tractography in crossing fiber regions. Int. J. Imag. Syst. Tech. **22**, 53–66 (2012)
13. Tuch, D.S.: Q-ball imaging. Magn. Reson. Med. **52**, 1358–1372 (2004)
14. Yeh, F.C., Wedeen, V.J., Tseng, W.Y.: Generalized q-sampling imaging. IEEE Trans. Med. Imag. **29**, 1626–1635 (2010)